Supplement to March /April 2024
Volume 53, Number 2

AppliedRadiology®

The Journal of Practical Medical Imaging and Management

Pediatric Imaging Case Series

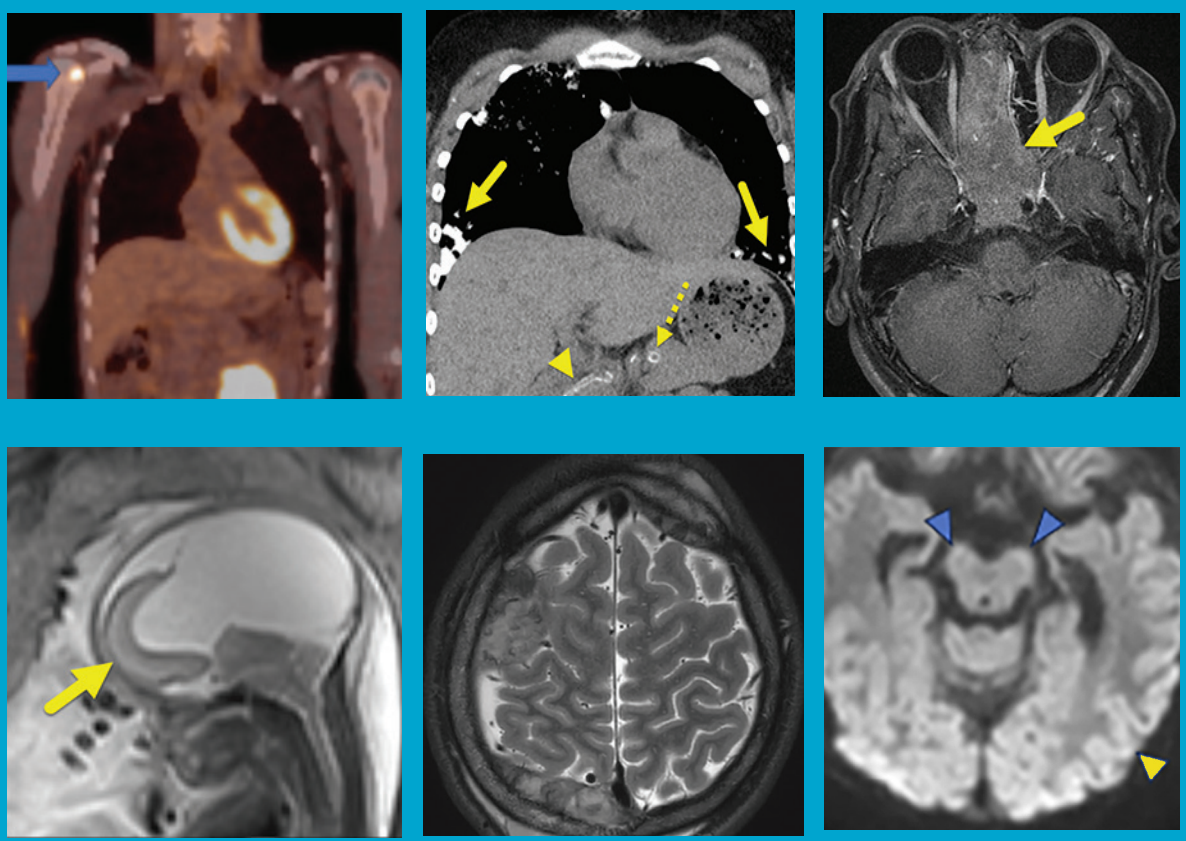

Retroperitoneal Paraganglioma | Metastatic Pulmonary Calcinosis | Craniofacial Fibrous Dysplasia | Alobar Holoprosencephaly | Ewing Sarcoma | Acute Wallerian Degeneration |

Applied Radiology®

The Journal of Practical Medical Imaging and Management

Anderson Publishing, Ltd
180 Glenside Avenue,
Scotch Plains, NJ 07076
Tel: 908-301-1995
Fax: 908-301-1997
info@appliedradiology.com

Contents

Retroperitoneal Paraganglioma

Jayden T. Gubler, ; Richard B. Towbin, MD; Carrie M. Schaefer, MD; Alexander J. Towbin, MD

Case Summary

A heathy teenager presented with left flank pain and dizziness after a collision with another player during a sporting event. Physical examination revealed diffuse left flank tenderness without ecchymosis. Vital signs were stable, with a blood pressure of 113/65 and heart rate of 66 bpm. Hemoglobin and hematocrit were normal.

Imaging Findings

CT of the abdomen and pelvis demonstrated an enhancing, 7.5 cm, left retroperitoneal mass with central hypodensity, and a left perinephric and retroperitoneal hematoma (Figure 1). PET/CT showed uptake in the retroperitoneal mass with a maximum SUV of 15.6 and fluorodeoxyglucose-avid metastases to the skull, thoracic spine, and right humerus (Figure 2). The tumor type was confirmed preoperatively with an image-guided percutaneous biopsy.

Diagnosis

Retroperitoneal paraganglioma (PGL).

The differential diagnoses include lymphoma, metastasis (such as from a testicular tumor), and sarcoma.

Discussion

Paragangliomas and pheochromocytomas are rare primary retroperitoneal tumors composed of neuroendocrine cells, or chromaffin cells, that arise from neural crest cells known as pheochromoblasts. PGL arises in extra-adrenal sites, while pheochromocytoma arises in the adrenal medulla. The first documented PGL was described by Alezais and Peyron in 1908.[1]

It has been estimated that PGLs and pheochromocytomas occur in roughly 2-8 per 1 million people each year.[2] PGLs can occur anywhere paraganglia are located, commonly in parasympathetic tissue in the head, neck, and thorax, or in sympathetic tissue in the abdomen and pelvis. PGLs most often occur sporadically, but approximately one-third are associated with genetic factors including von Hippel-Lindau Syndrome, multiple endocrine neoplasia types 2A and 2B, neurofibromatosis type 1, and succinate dehydrogenase complex mutations. Genetic testing can therefore be useful in diagnosing and managing suspected PGLs.

Clinical features are often related to the effects of the products of the tumor; namely excess catecholamines. Symptoms will fluctuate based on the levels of epinephrine, norepinephrine, and dopamine, and are therefore relapsing and remitting in nature. PGLs can present with symptoms classically described as the 5 P's: increased blood pressure, head pain (headache), perspiration, palpitations, and pallor. Other less-specific features include abdominal pain, anxiety, weight loss, and hyperglycemia. However, 20-30% or more of patients with PGLs have only minor signs or are asymptomatic, resulting in underdiagnosis.[1]

Diagnosing PGL relies on laboratory tests and imaging. Initially, plasma free-metanephrine tests such as homovanillic acid or vanillylmandelic acid can be utilized. A more specific and definitive biochemical approach is to test for metanephrines and catecholamines in a 24-hour urine specimen, with urinary

Affiliations: University of Arizona College of Medicine-Phoenix Campus (Mr Gubler); Department of Radiology, Phoenix Children's Hospital (Drs Schaefer, R. Towbin); Children's Hospital Medical Center, Cincinnati, University of Cincinnati College of Medicine (Dr A. Towbin)

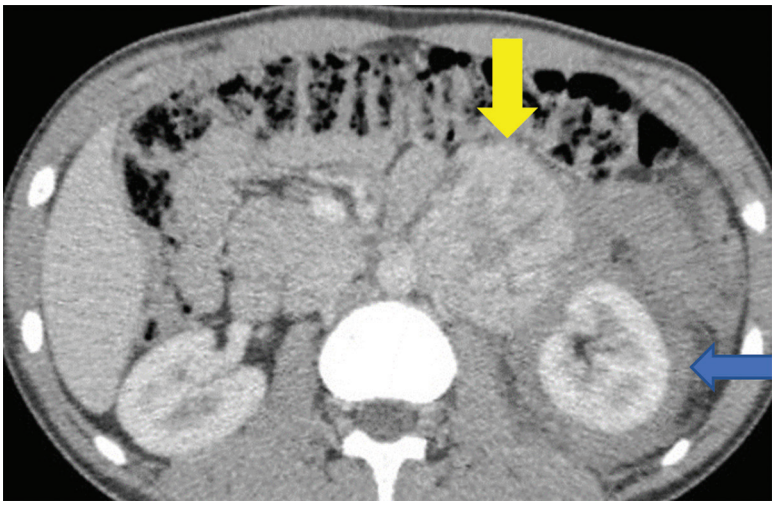

Figure 1. Contrast-enhanced CT of the abdomen demonstrates a heterogeneous left retroperitoneal mass (yellow arrow) anterior to the left kidney and psoas muscle, as well as a left perinephric/retroperitoneal hematoma (blue arrow).

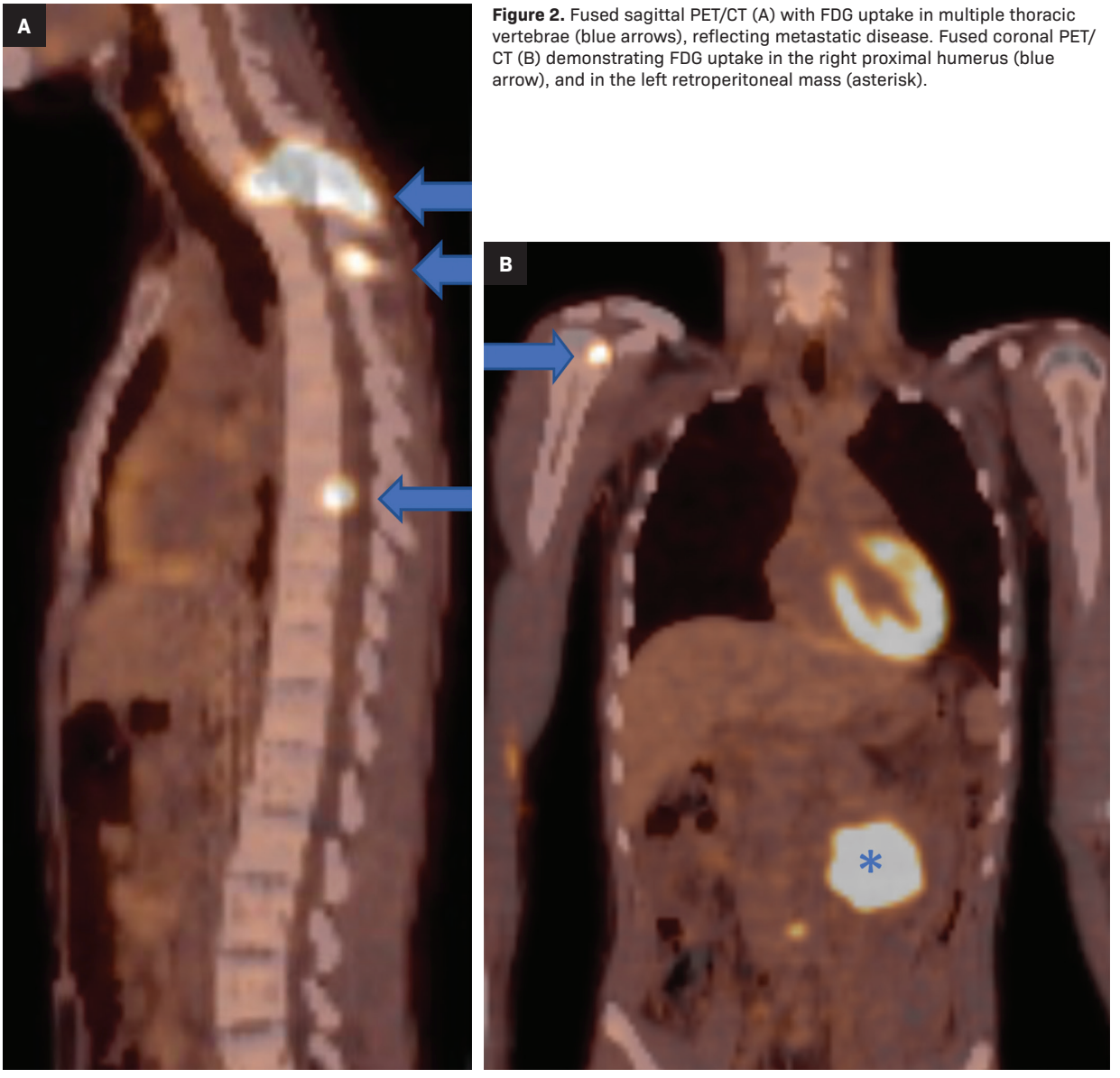

Figure 2. Fused sagittal PET/CT (A) with FDG uptake in multiple thoracic vertebrae (blue arrows), reflecting metastatic disease. Fused coronal PET/CT (B) demonstrating FDG uptake in the right proximal humerus (blue arrow), and in the left retroperitoneal mass (asterisk).

vanillylmandelic acid having a 95% specificity.[3] After a diagnosis of PGL is established, imaging is used to localize the tumor.

Several imaging modalities can be used to localize PGL. These include CT, MRI, single-photon emission computed tomography (SPECT) using ^{123}I-metaiodobenzylguanidine (^{123}I-MIBG) or ^{111}In-DTPA-pentetreotide, and positron emission tomography using 6-[^{18}F]-fluorodopamine (^{18}F-FDA), 6-[^{18}F]-fluoro-L-3,4-dihydroxyphenylalanine, and 2-[^{18}F]-fluoro-2-deoxy-D-glucose (^{18}F-FDG).

Of these modalities, CT or MRI is considered first line. These approaches provide high sensitivity and typically find the tumor. Computed tomography of the neck, chest, abdomen, and pelvis is often used to identify the primary tumor and to assess for metastasis.

Coupling anatomical imaging with functional imaging specific to PGLs is necessary to provide specificity. Nuclear medicine scanning is especially useful owing to the unique characteristics of PGLs in taking up specific radiotracers. The use of ^{18}F-FDG PET or ^{18}F-FDA PET for suspected metastasis and ^{123}I-MIBG SPECT for established metastasis are most useful; however, other markers should be considered based on the entire clinical picture.[4]

Approximately 25% of PGLs are malignant.[5] Malignancy is determined by the tumor's behavior; ie, metastasis to non-chromaffin tissue, and not necessarily its histology. Histology of PGLs, though, typically shows circumscribed nests of polyhedral to fusiform neoplastic cells, known as "zellballen," that contain granular, amphophilic or basophilic cytoplasm and vesicular nuclei.[6]

Prediction of malignancy is often difficult and involves several risk factors and a scoring system. Risk factors include succinate dehydrogenase complex gene mutations, primary tumor size, younger age, and elevated 3-Methoxytyramine levels. The most extensively used scoring system is Grading of Adrenal Pheochromocytoma and Paraganglioma which grades PGLs as low, intermediate, or high risk for metastasis. Malignant PGLs typically spread to regional cervical lymph nodes or distant locations such as the bone, liver, and lungs, depending on their primary location above or below the neck, respectively.[2]

Treatment options and prognosis depend on whether the tumor is benign or malignant. Surgical removal is definitive for benign lesions; however, metastatic tumors are more complicated and often involve control of symptoms and tumor growth. Percutaneous image-guided biopsy may be valuable in confirming the diagnosis. However, it is essential to block the catecholamine effect before biopsy.

Symptomatic control for both benign and metastatic PGLs is obtained first by alpha and, when indicated, beta-adrenergic blockade. Phenoxybenzamine is a long-acting, nonselective, noncompetitive alpha-adrenergic blocker and is the most commonly used agent, followed by doxazosin, a selective alpha-1-adrenergic blocker. Slowly progressive tumors are sometimes monitored in cases of asymptomatic metastatic PGLs, but they require intensive lab and radiological following.[7]

Surgical resection is often not curative in metastatic PGLs; however, it is useful in controlling symptoms. Total surgical resection of the primary tumor, regional lymph nodes, and distant metastases is the preferred method. Radiofrequency ablation and direct intra-tumoral injection of absolute alcohol into unresectable tumors is also an option. Chemotherapy, molecular targeted therapy, and radionuclide therapy are often used in combination with multiple forms of treatment for adequate systemic therapy.

Prognosis in cases of metastases to the liver and lungs is generally poor, with shorter survival compared to metastases to the bone. Metastases to the bone develop in roughly 70% of these cases. These are mainly lytic lesions and require combination therapy with medications such as bisphosphonates or RANKL inhibitors, irradiation, and radiofrequency ablation.[7]

Long-term follow-up is required with any PGL or pheochromocytoma. Biochemical testing is performed to confirm complete tumor resection and further biochemical assays are used to monitor recurrence. Recurrence rates ranging from 14% to 30% have been documented, and malignancy is seen in half of recurrences.[2,5] Therefore, life-long follow-up of these patients is appropriate.

References

1) Kantorovich V, Pacak K. Pheochromocytoma and Paraganglioma. In: *Progress in Brain Research*. Vol 182. Elsevier; 2010:343-373. doi:10.1016/S0079-6123(10)82015-1

2) Pacak K, Tella SH. Pheochromocytoma and Paraganglioma. In: Feingold KR, Anawalt B, Boyce A, et al., eds. *Endotext*. MDText.com, Inc.; 2000. Accessed April 16, 2022. http://www.ncbi.nlm.nih.gov/books/NBK481899/

3) Lenders JWM, Pacak K, Walther MM, et al. Biochemical diagnosis of pheochromocytoma: which test is best? *JAMA*. 2002;287(11):1427-1434. doi:10.1001/jama.287.11.1427

4) Timmers HJLM, Taieb D, Pacak K. Current and Future Anatomical and Functional Imaging Approaches to Pheochromocytoma and Paraganglioma. *Horm Metab Res Horm Stoffwechselforschung Horm Metab*. 2012;44(5):367-372. doi:10.1055/s-0031-1299712

5) Wang H, Jepegnanam C. Recognition and management of phaeochromocytoma and paraganglioma. *Anaesth Intensive Care Med*. 2017;18(10):496-501. doi:10.1016/j.mpaic.2017.06.022

6) Merino MJ., Klimstra DS, Stelow EB, Strayer DS, Rubin E, Williams KJ, Siraj ES. The Endocrine System, Chapter 27, pages 647-695. *Rubin's Pathology: Clinicopathologic Foundations of Medicine*. Seventh edition. Wolters Kluwer Health; 2015.

7) Angelousi A, Kassi E, Zografos G, Kaltsas G. Metastatic pheochromocytoma and paraganglioma. *Eur J Clin Invest*. 2015;45(9):986-997. doi:10.1111/eci.12495

Metastatic Pulmonary Calcinosis

Vishal Jindal, MD; Alexander J. Towbin, MD; Daniel Morgan; Richard B. Towbin, MD

Case Summary

A teenager with a history of antineutrophil cytoplasmic autoantibody (ANCA)-associated vasculitis, pulmonary hemorrhage, and renal failure presented with a mild chronic cough and superficial thrombophlebitis. At laboratory examination their calcium level was 10.4 mg/dL (normal 8.7-10.8 mg/dL) and serum phosphate was 9.8 mg/dL (normal 3.1-5.4 mg/dL).

Imaging Findings

The initial CT scan (Figure 1) demonstrated extensive nodular opacities concentrated in a peripheral distribution throughout the lungs. The opacities had areas of increased density, which were that of calcification. Follow-up CT performed 18 months later (Figure 2) showed improvement in the calcifications and development of cysts in areas of prior calcification.

Affiliations: Touro University College of Osteopathic Medicine (Dr Jindal), Department of Radiology, Cincinnati Children's Hospital (Dr A Towbin); University of Cincinnati College of Medicine (Drs Morgan, A Towbin), Department of Radiology, Phoenix Children's Hospital (Dr R Towbin)

Diagnosis

Metastatic pulmonary calcinosis secondary to renal failure. The differential diagnosis includes idiopathic pulmonary ossification, ossified pulmonary metastasis, chronic hemorrhagic conditions, infection, and inflammatory disorders.

Discussion

Metastatic pulmonary calcinosis (MPC) is a lung disease characterized by calcifications in the pulmonary parenchyma. It commonly occurs in patients with chronic renal failure. Studies have shown that 60 to 75% of patients on hemodialysis had MPC on autopsy yet were asymptomatic during life.[1,2] While the diagnosis is relatively common in adults with chronic renal failure, it is rare in children and very few cases have been reported.[3]

Patients with MPC are usually asymptomatic but can report a chronic, nonproductive cough and respiratory distress. There is no association between the level of respiratory distress and the extent of calcifications.[2,4,5]

Metastatic calcification can occur in normal tissue when the calcium-phosphate product (serum Ca * serum P) is greater than 70 mg^2/dL^2 (normal < 40 mg^2/dL^2).[2,5] This elevation occurs most often in patients with renal failure. While the calcium-phosphate product can be elevated in other conditions such as primary hyperparathyroidism, tumors, renal or liver transplantation, and following cardiac surgery, the level in these conditions is generally below 60 mg^2/dL^2 and MPC does not occur.[2,6]

Metastatic calcinosis can also affect the kidneys and stomach, although the lungs are the most commonly affected organs.[1,2] They have an alkaline environment, as they secrete free hydrogen ion, allowing for the formation of calcium salts. The calcifications occur in the interstitium of the alveolar septa, the walls of the bronchioles, or large airways. The upper lobes are affected more often than the lower lungs, owing to the former's higher ventilation/perfusion ratio, which leads to higher pH levels.[4,6,7]

Chest radiography is not sensitive to MPC. Most patients have normal radiographs owing to low levels of calcium deposition.[2,4,8] In one study of seven patients with MPC, calcifications were visible on chest

Figure 1. (A) Axial and (B) coronal noncontrast chest CT shows metastatic calcification (arrows) in both lungs, predominately peripherally. (C) Coronal image displayed in soft-tissue windows shows metastatic calcification (arrows), calcification of the hepatic artery (arrowhead), and calcification of the splenic artery (dashed arrow).

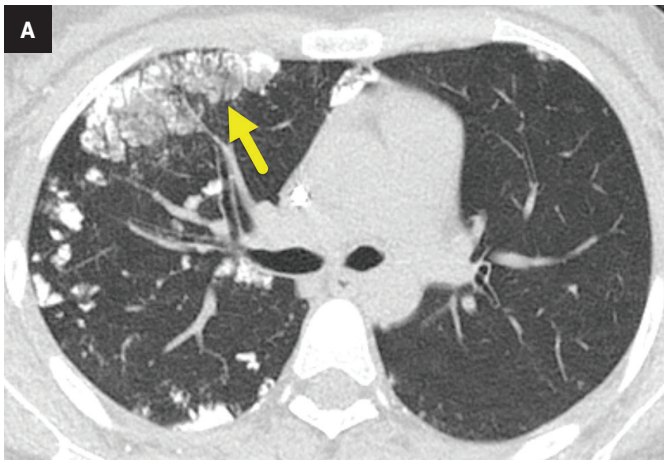

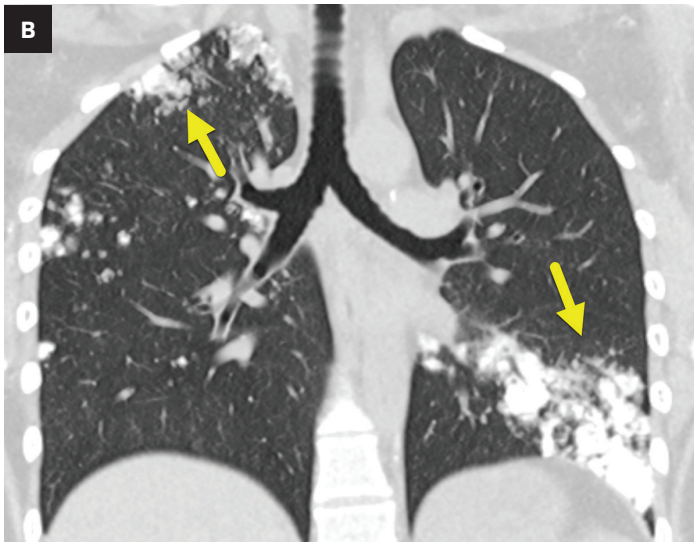

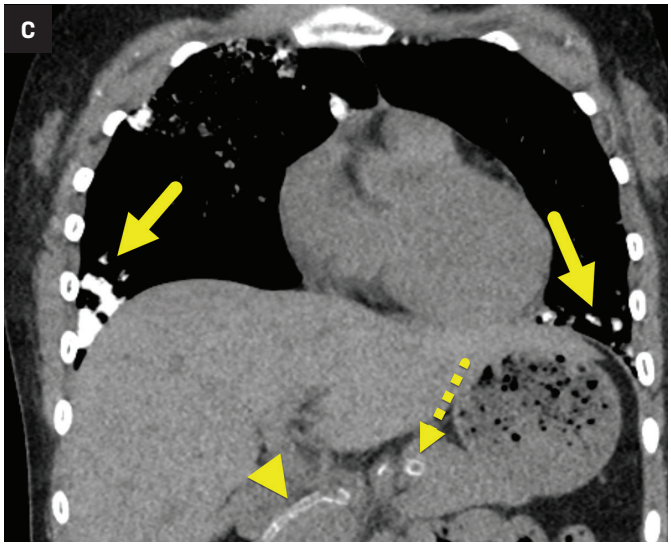

Figure 2. (A) Axial and (B) coronal noncontrast chest CT performed 18 months after that presented in Figure 1 shows a substantial post-treatment decrease in MPC. However, some dense calcifications remain. Additionally, some of the lung parenchyma that was previously calcified (arrow) now has a cystic appearance.

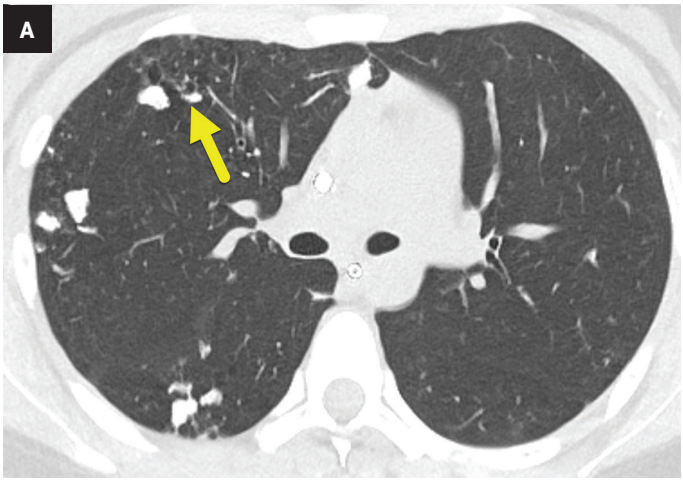

radiographs in only two and on CT in all seven.[9] When visible on radiographs, the calcifications can appear as regions of consolidation.

High-resolution chest CT is preferred for diagnosing MPC.[8] Three patterns have been described: diffuse or patchy areas of ground-glass opacity or consolidation; multiple diffuse calcified nodules; and confluent high-attenuation parenchymal consolidation. Of these, centrilobular ground-glass opacities that may contain foci of calcification are the most common.[2,4,10] Other findings associated with MPC include calcification of the chest wall vessels, myocardium, bronchial wall, small pulmonary arteries, and the superior vena cava.[2]

Technetium 99m-methyl diphosphonate bone scintigraphy has shown to be effective for early detection of MPC. Affected lungs show regional increased radiotracer uptake.[3,11] MPC can also be detected on MRI. On T1 images, MPC appears hyperintense compared to muscle and has a higher lesion/muscle signal intensity ratio compared to that of T2 images.[2] Although MRI can show metastatic calcinosis, it is often not used because of its lower sensitivity for detection.

The pulmonary prognosis for most patients is good. The goal of treatment is to normalize serum levels of calcium and phosphate.[2,6,8] Commonly used medications include bisphosphonates, phosphate binders, and vitamin D supplementation. In more advanced disease, parathyroidectomy, increased dialysis, or renal transplant may be considered.[6,10] As calcium and phosphate levels normalize, calcium deposition in the lungs may decrease and pulmonary function may increase.[2,6,10] This was the case in our patient.

Conclusion

Metastatic pulmonary calcinosis is a rare condition seen mostly in patients with renal failure. Affected patients are often asymptomatic but can develop respiratory distress. Diagnosis is typically made with chest CT, which demonstrates centrilobular ground-glass opacities that may contain foci of calcification. Treatment involves normalizing calcium and phosphate serum levels and possible surgical intervention.

References

1) Conger JD, Hammond WS, Alfrey AC, Contiguglia SR, Stanford RE, Huffer WE. Pulmonary calcification in chronic dialysis patients. Clinical and pathologic studies. *Ann Intern Med*. 1975;;83(3):330-336. doi: 10.7326/0003-4819-83-3-330. PMID: 1190631.

2) Belém LC, Zanetti G, Souza AS Jr, et al. Metastatic pulmonary calcification: state-of-the-art review focused on imaging findings. *Respir Med*. 2014 ;108(5):668-676. doi: 10.1016/j.rmed.2014.01.012. Epub 2014 Feb 6. PMID: 24529738.

3) Ueno K, Shimizu M, Uchiyama A, Hatasaki K. Fulminant respiratory failure due to progressive metastatic pulmonary calcification with no predisposing factors after successful renal transplantation: A case report. *Pediatr Transplant*. 2016; 20(8):1152-1156. doi: 10.1111/petr.12829. Epub 2016 Sep 27. PMID: 27671225..

4) Bendayan D, Barziv Y, Kramer MR. Pulmonary calcifications: a review. *Respir Med*. 2000; 94(3):190-193. doi: 10.1053/rmed.1999.0716. PMID: 10783928.

5) Sun HM, Chen F, Yin HL, Xu XY, Liu HB, Zhao BL. Rapid development of metastatic pulmonary calcifications in primary hyperparathyroidism: a case report and literature review. *Diagn Pathol*. 2017; 8;12(1):38. doi: 10.1186/s13000-017-0628-1. PMID: 28482911; PMCID: PMC5423015.

6) Pinto JF, Schmitt W, Fernandes C, Franca M. Metastatic pulmonary calcifications: a complication of chronic renal disease. *Acta Radiologica Portuguesa*. 2022; 33(3) 31-34.

7) Jost RG, Sagel SS. Metastatic calcification in the lung apex. *AJR Am J Roentgenol*. 1979;133(6):1188-1190. doi: 10.2214/ajr.133.6.1188. PMID: 116518.

8) Thurley PD, Duerden R, Roe S, Pointon K. Case report: Rapidly progressive metastatic pulmonary calcification: evolution of changes on CT. *Br J Radiol*. 2009; 82(980):e155-159. doi: 10.1259/bjr/87606661. PMID: 19592398.

9) Hartman TE, Müller NL, Primack SL, Johkoh T, Takeuchi N, Ikezoe J, Swensen SJ. Metastatic pulmonary calcification in patients with hypercalcemia: findings on chest radiographs and CT scans. *AJR Am J Roentgenol*. 1994; 162(4):799-802. doi: 10.2214/ajr.162.4.8140993. PMID: 8140993.

10) Michali-Stolarska M, Zacharzewska-Gondek A, Bladowska J, Guziński M, Sąsiadek MJ. Metastatic pulmonary calcification as a rare complication of end-stage renal disease with coexistence of pulmonary metastases from renal cell carcinoma: case report and literature review. *Pol J Radiol*. 2018; 83: e115-e119. doi: 10.5114/pjr.2018.75725. PMID: 30038687; PMCID: PMC6047097.

11) Brodeur FJ Jr, Kazerooni EA. Metastatic pulmonary calcification mimicking air-space disease. Technetium-99m-MDP SPECT imaging. *Chest*. 1994;106(2):620-622. doi: 10.1378/chest.106.2.620. PMID: 7774354.

Craniofacial Fibrous Dysplasia

Ala'a Abu Zaineh; Richard B. Towbin, MD; Carrie M. Schaefer, MD; Alexander J. Towbin, MD

Case Summary

A young teenager presented with concerns of decreased vision in the right eye. The patient was noted to have right-sided diplopia and facial asymmetry. Ophthalmologic examination showed right optic nerve pallor and constricted visual field with preserved vision nasally and a dense right afferent pupillary defect.

Imaging findings

Brain MRI (Figure 1) demonstrated expansion of the right frontal bone, orbital roof, lesser sphenoid wing and body, ethmoid septae, and cribriform plate with stenosis of the right optic canal. Head CT (Figure 2) showed extensive bony thickening with a "ground-glass" appearance and causing narrowing of the right optic canal.

Diagnosis

Craniofacial fibrous dysplasia.

Affiliations: Faculty of Medicine of Setif, Algeria (Dr Abu Zaineh); Department of Radiology, Phoenix Children's Hospital, Phoenix, Arizona (Drs R. Towbin, Schaefer); Department of Radiology, Children's Hospital Medical Center, Cincinnati, Ohio; Department of Radiology, University of Cincinnati College of Medicine (Dr A Towbin)

Discussion

Fibrous dysplasia is a congenital, non-inherited skeletal dysplasia characterized by the replacement of normal bone and marrow with fibrous bone tissue and poorly formed trabecular bone.[1,2] It is caused by somatic activating mutations in the alpha subunit of the stimulatory G protein encoded by the gene GNAS, resulting in abnormal osteogenesis.[3] Fibrous dysplasia may involve one bone (monostotic) or multiple bones (polyostotic). The former accounts for 75-80% of cases while the latter is seen in 20-25% of cases.[4] While fibrous dysplasia can affect any bone, the most common sites of monostotic disease are the ribs (28%), proximal femur (23%), tibia, and craniofacial bones, especially the posterior maxilla.[5,6] Fibrous dysplasia that only affects the bones of the face and/or skull is referred to as craniofacial fibrous dysplasia.

Monostotic lesions are typically asymptomatic and may progress during skeletal growth and stabilize after puberty; however, they may continue enlarging in adulthood. Pregnancy can cause increased growth of the lesion, as well as secondary changes of aneurysmal bone cyst formation. Complications of fibrous dysplasia result mainly from secondary compression and/or displacement of adjacent structures. In craniofacial fibrous dysplasia, the bone lesions lead to compression of the cranial nerves and/or the orbit. Up to half of patients may develop bone fracture as a complication.

Polyostotic forms are distinguished by early onset and rapid progression. They may involve adjacent bones of a single body area or almost the entire skeleton. The bones most affected are the femur (91%), tibia (81%), pelvis, feet, skull, and facial bones.[7]

Polyostotic fibrous dysplasia can occur alone or as part of a genetic syndrome.[8] McCune-Albright syndrome consists of polyostotic fibrous dysplasia, autonomous endocrine hyperfunction, and café-au-lait skin pigmentation. Patients who have fibrous dysplasia associated with McCune-Albright syndrome usually present with skin lesions along the midline of the body and include jaggedly bordered macules. In this setting, fibrous dysplasia typically manifests in early infancy, with the classic "Shepherd crook" coxa vara deformity. Precocious puberty is the most common manifestation of the syndrome in females. Rare, but severe, extraskeletal complications

Figure 1. Axial T1 (A), T2 (B), and T1 postcontrast (C) MRI at the level of the ethmoid air cells show an expansile mass filling the right ethmoid sinus. Axial T1 (D), T2 (E), and T1 postcontrast (F) MRI at the level of the frontal bone shows extension of the lesion to the right frontal bone. The lesion is mildly hyperintense compared to adjacent bone on the T1 images, is hypointense on T2 images, and enhances heterogeneously.

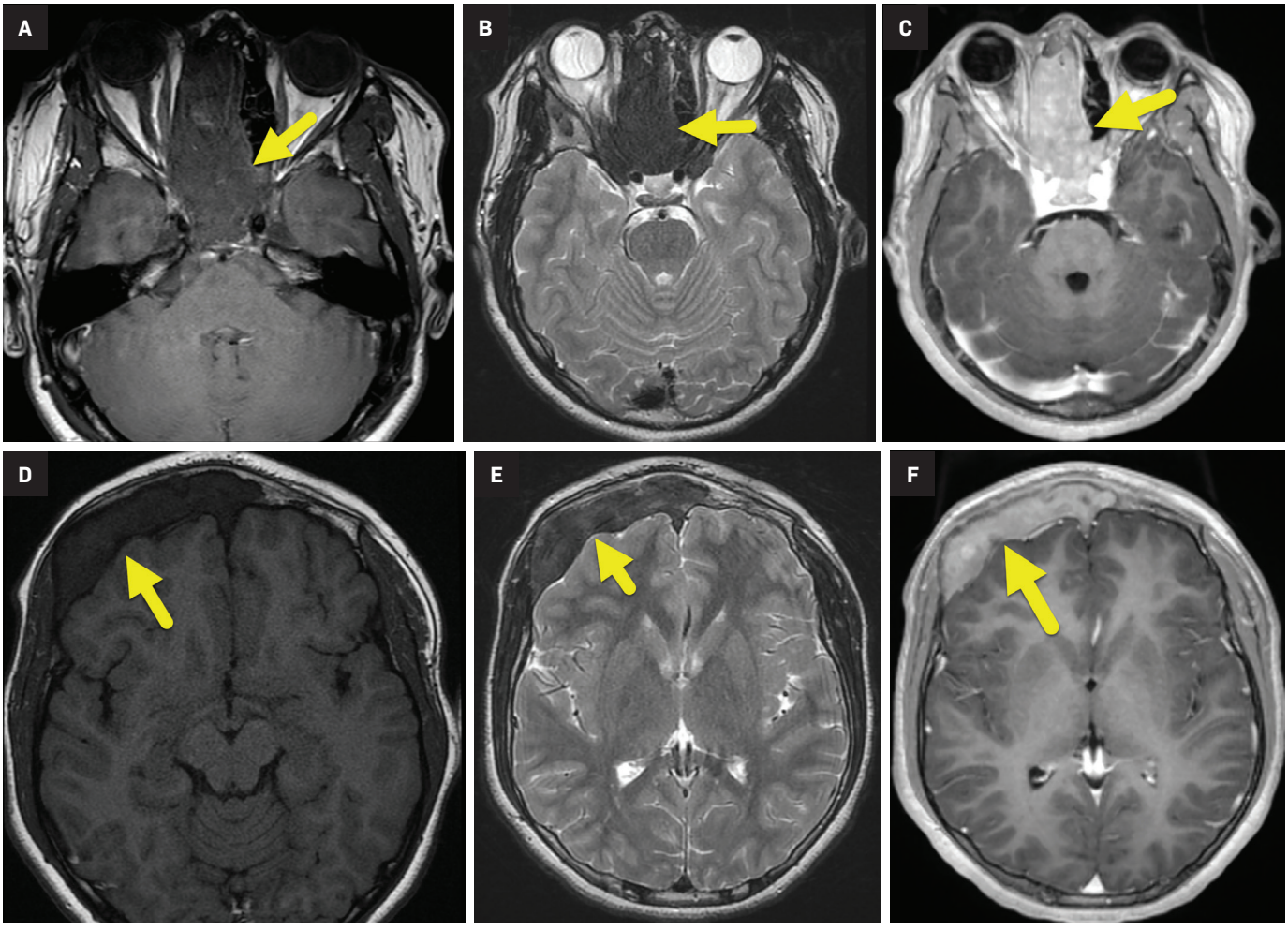

Figure 2. Axial CT images at the level of the ethmoid air cells (A), sphenoid wing (B), and frontal bone (C) demonstrate an expansile sclerotic lesion with a ground-glass matrix extending from the right ethmoid air cells through the right frontal bone.

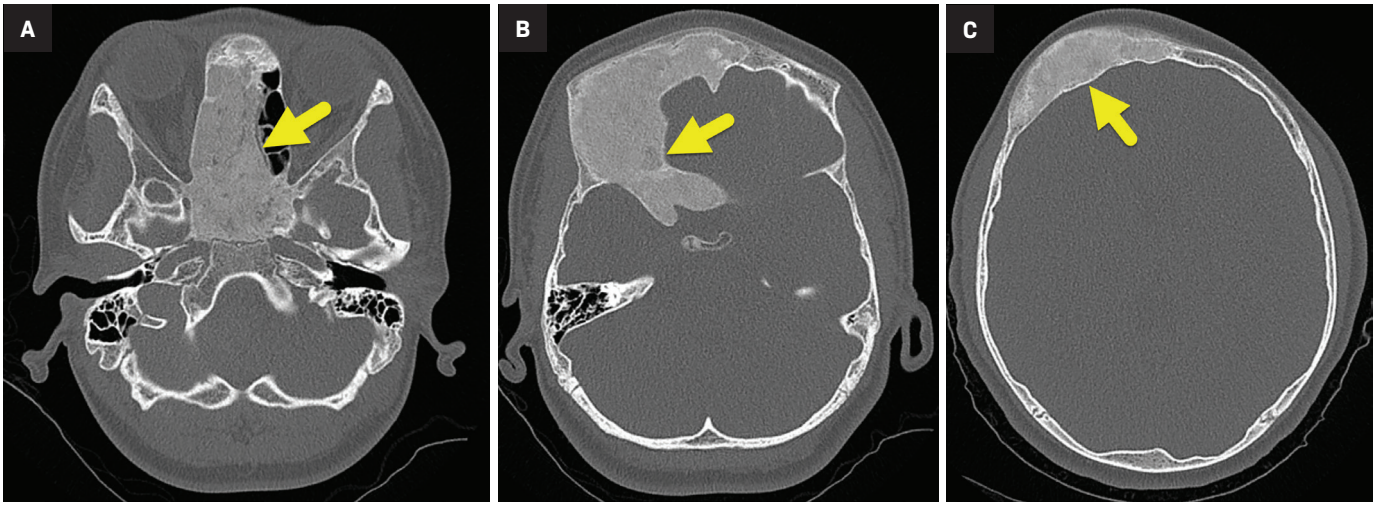

may occur, ranging from gastrointestinal reflux to cardiac arrhythmias and sudden death.

Milder forms of fibrous dysplasia may be asymptomatic and only discovered incidentally. The most common symptoms are bone pain and swelling; in severe cases, especially in the polyostotic form, fractures and bone deformity may occur. Rarely, malignant transformation occurs with the development of fibrosarcoma, chondrosarcoma, osteosarcoma, or malignant fibrous histiocytoma.

On radiographs, fibrous dysplasia typically appears as an intramedullary, expansile, well-defined, lucent lesion in the metaphysis or diaphysis, with no periosteal reaction. Most lesions have a characteristic hazy, ground-glass matrix. However, some may appear entirely lucent or sclerotic. In addition, they may be surrounded by a layer of thick, sclerotic reactive bone termed a "rind." The degree of matrix at radiography correlates directly with its underlying histopathology.

More radiolucent lesions are composed predominantly of fibrous elements, whereas more radiopaque lesions contain a greater proportion of woven bone. The ribs may have a bubbly cystic appearance with fusiform enlargement. Involvement of the lower extremities can lead to bowing deformities, shepherd crook deformity of the femoral neck, looser zones, or premature fusion of growth plates, resulting in short stature or limb length discrepancy.

On CT, the lesion most commonly appears expansile with a ground-glass matrix and well-defined borders. Again, some lesions may appear more lucent or sclerotic. Magnetic resonance imaging can help to characterize the secondary effects on adjacent structures.[9] Because fibrous dysplasia is composed mainly of fibrous tissue and bone, T1 images typically have a low-intensity signal, while T2 images are mixed. Most commonly T2-weighted imaging have a higher intensity signal that is not as bright as fluid. However, some lesions can have diffuse low T2 signal. T1, postcontrast images typically show heterogeneous contrast enhancement in affected areas.

Technetium 99m-methyl diphosphonate bone scanning may be used to gauge the extent of disease at initial presentation. Active fibrous dysplasia lesions in younger patients have greatly increased radiotracer uptake. The uptake becomes less intense as the lesions mature.

Conclusion

Fibrous dysplasia is a congenital, non-inherited skeletal disorder characterized by replacement of normal bone with fibrous bone tissue and poorly formed trabecular bone. Milder forms of the disease may not cause symptoms, while more severe forms may result in complications related to weakened bone or compression/displacement of adjacent structures. Fibrous dysplasia may be seen in all modalities, and treatment should be tailored to the needs of the patient.

References

1) Burke AB, Collins MT, Boyce AM. Fibrous dysplasia of bone: craniofacial and dental implications. *Oral Dis*. 2017;23(6):697-708. doi:10.1111/ODI.12563

2) Lee JS, Fitzgibbon EJ, Chen YR, et al. Clinical guidelines for the management of craniofacial fibrous dysplasia. *Orphanet J Rare Dis*. 2012;7(SUPPL. 1). doi:10.1186/1750-1172-7-S1-S2

3) Schwindinger WF, Francomano CA, Levine MA. Identification of a mutation in the gene encoding the α subunit of the stimulatory G protein of adenylyl cyclase in McCune-Albright syndrome. *Proc Natl Acad Sci U S A*. 1992;89(11):5152-5156. doi:10.1073/PNAS.89.11.5152

4) Riddle ND, Bui MM. Fibrous dysplasia. *Arch Pathol Lab Med*. 2013;137(1):134-138. doi:10.5858/ARPA.2012.0013-RS

5) Godse AS, Shrotriya SP, Vaid NS. Fibrous dysplasia of the maxilla. *J Pediatr Surg*. 2009;44(4):849-851. doi:10.1016/J.JPEDSURG.2008.12.006

6) Rahman AMA, Madge SN, Billing K, et al. Craniofacial fibrous dysplasia: clinical characteristics and long-term outcomes. *Eye (Lond)*. 2009;23(12):2175-2181. doi:10.1038/EYE.2009.6

7) Value of (99m)Tc-MDP SPECT/CT and (18) F-FDG PET/CT scanning in the evaluation of malignantly transformed fibrous dysplasia | Read by QxMD. Accessed December 20, 2022. https://read.qxmd.com/read/28721303/value-of-99m-tc-mdp-spect-ct-and-18-f-fdg-pet-ct-scanning-in-the-evaluation-of-malignantly-transformed-fibrous-dysplasia

8) Boyce AM, Florenzano P, Castro LF de, Collins MT. Fibrous Dysplasia/McCune-Albright Syndrome. *GeneReviews(R)*. Published online June 27, 2019. Accessed January 3, 2022. https://www.ncbi.nlm.nih.gov/books/NBK274564/

9) Wootton-Gorges SL. MR imaging of primary bone tumors and tumor-like conditions in children. *Magn Reson Imaging Clin N Am*. 2009;17(3):469-487. doi:10.1016/J.MRIC.2009.03.010

Alobar Holoprosencephaly

Amaris Tapia; Richard B. Towbin, MD; Carrie M. Schaefer, MD; Alexander J. Towbin, MD

Case Summary

A routine obstetrical ultrasound detected multiple fetal brain and facial anomalies, as well as macrosomia, macrocephaly, and polyhydramnios, prompting further evaluation. Subsequent fetal MRI demonstrated severe brain and facial developmental abnormalities. A fetal echocardiogram was normal.

A liveborn infant was delivered via scheduled C-section. The neonate required intubation for respiratory failure and was found to have multiple endocrinopathies, including central diabetes insipidus, hypoglycemia, hypothyroidism, and growth hormone deficiency secondary to panhypopituitarism. The baby developed hypotension, persistent seizure activity, and worsening metabolic acidosis with episodes of prolonged bradycardia. Owing to declining clinical status, care was withdrawn.

Affiliations: University of Arizona College of Medicine-Phoenix Campus (Ms Tapia), Department of Radiology, Phoenix Children's Hospital, (Drs Schaefer, R. Towbin), Department of Radiology, Cincinnati Children's Hospital, University of Cincinnati College of Medicine (Dr A. Towbin)

Imaging Findings

Fetal MRI (Figure 1) showed features of alobar holoprosencephaly (HPE), including failure of separation of the cerebral hemispheres and thalami, absence of normal supratentorial sulci, and a dilated supratentorial monoventricle communicating with a large dorsal cyst that caused mass effect on the posterior cranial fossa. The brainstem was severely dysplastic with incomplete segmentation between the thalami and the midbrain. There were midline cleft lip/palate and arrhinia with hypoplasia of the nasal cavity. Fetal eyes were not identified, suggesting severe bilateral microphthalmia or anophthalmia.

A postnatal head ultrasound (Figure 2) demonstrated a large monoventricle with absence of the corpus callosum, interhemispheric fissure, and cavum septum pellucidum.

Brain MRI (Figure 3) showed intracranial findings of alobar HPE with fusion of frontal lobe parenchyma and the thalami, partial fusion of the midbrain, and absence of supratentorial midline structures. Additionally, there were features of macrocephaly and suspected aqueductal stenosis. The mass effect caused compression of posterior fossa structures with downward tonsillar herniation into the cervical canal. The impaction of the cerebellar tonsils was worsened by marked stenosis at the craniocervical junction. Dysmorphic orbital and facial structures were noted, with cephaloceles extending into the orbits.

Diagnosis

Alobar Holoprosencephaly.

Differential diagnosis includes other subtypes of HPE: lobar, semilobar, and the middle interhemispheric variant.[1]

Discussion

Holoprosencephaly is a brain malformation that results from failed or incomplete division of the forebrain (prosencephalon) into right and left cerebral hemispheres between the 18th and 28th day of gestation.[2] Incomplete separation of deep grey nuclei (thalami, hypothalamic nuclei, and basal ganglia) and malformation of cerebral ventricles is seen. HPE is estimated to occur in 1.31 of 10 000 live and stillbirths.[3]

Figure 1. Sagittal single shot fast spin echo image from fetal MRI (A) shows an agyric, fused frontal brain tissue (arrow) and a large dorsal cyst. Axial image (B) shows the low volume, fused cerebral parenchymal (arrow). Coronal image (C) highlights the agyric, fused parenchyma (arrow) and a large mono ventricle.

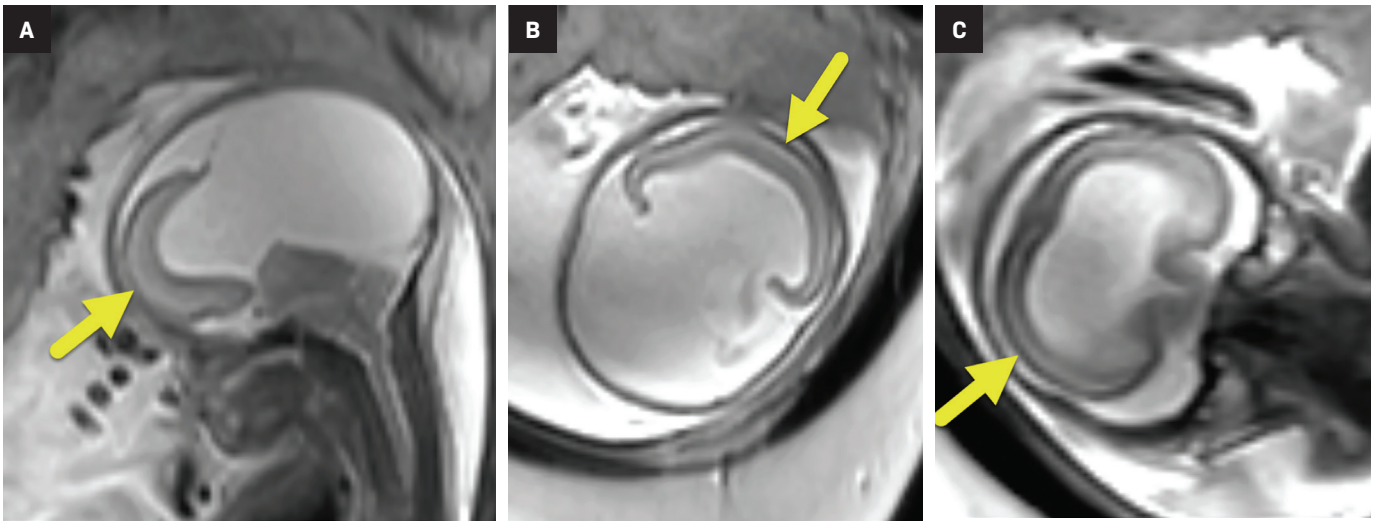

Historically, HPE was classified into DeMyer's three major subtypes based on severity: alobar, semilobar, and lobar HPE.[4] A nonclassical subtype of HPE, known as the middle interhemispheric fusion variant, has since been characterized.[5]

Alobar HPE is the most severe form. Alobar HPE presents with complete or near complete nonseparation of the cerebral hemispheres and deep gray nuclei.[4,5] In *semilobar* HPE, the anterior cerebral hemispheres fail to separate, but there is partial separation of the cerebral hemispheres posteriorly.[4,5] Lobar HPE is the mildest subtype; the posterior cerebral hemispheres are separated and there is some separation of the anterior cerebral hemispheres.[4,5] In the middle interhemispheric variant, the anterior frontal and occipital lobes are separated, but the posterior frontal and parietal lobes are not; the deep gray nuclei are typically separated.[4,5]

Prenatal ultrasound of the face and falx cerebri is the primary approach to diagnosing HPE as early as the first trimester.[6,7] Fetal MRI provides greater detail of developing brain structures.[6,7] Postnatally, head ultrasound is often the first modality utilized, since it can be performed at bedside. However, brain MRI is the gold standard for diagnosis and subtyping of the HPE spectrum. Serial imaging may be necessary in patients with enlarging head size.[6]

Alobar HPE has characteristic brain MRI findings such as fusion of the cerebral hemispheres, basal ganglia, hypothalamic nuclei, and thalamic nuclei.[1,5] There is a single midline, crescent-shaped monoventricle that often communicates with a dorsal cyst.[1,4,5] The interhemispheric fissure, falx cerebri, corpus callosum, third ventricle and olfactory bulbs and tracts are absent.[1]

Newborns with alobar HPE commonly present with hypotonia, spasticity, and seizures.[1] Hydrocephalus and macrocephaly may also be seen, owing to the presence of a large dorsal cyst and/or aqueductal stenosis; however, microcephaly is also common.[1] Alobar HPE is often associated with a spectrum of severe midline craniofacial malformations. These include cyclopia with or without proboscis (tubular nose-like structure), ethmocephaly (separate orbits with proboscis), cebocephaly (closely spaced eyes with single-nostril nose), hypoplastic nose, hypotelorism, anophthalmia or microphthalmia, and bilateral cleft lip and palate.[1,5]

Figure 2. Postnatal ultrasound shows a large ventricle and fusion of the diencephalic-mesencephalic anlage. (arrow).

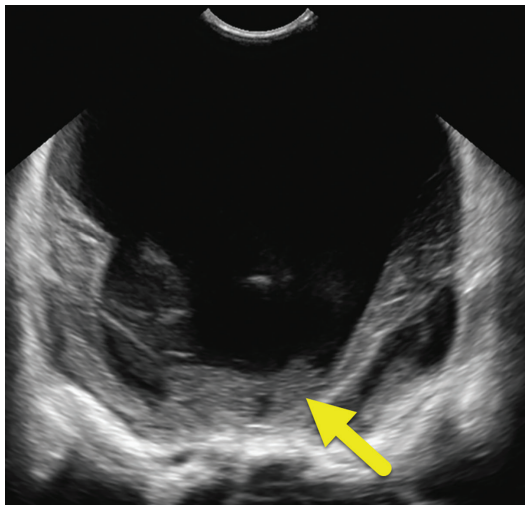

Patients with alobar HPE are more likely to develop hydrocephalus and may benefit from a cerebrospinal fluid shunt.[8] A gastrostomy tube is often placed to provide nutrition, as well as to reduce the risk of aspiration and recurrent lung infections.[8,9]

Alobar HPE is also associated with autonomic nervous system and hypothalamic dysfunction, which result in abnormal sleep-wake cycles,

Figure 3. Sagittal T2, postnatal brain MRI (A) shows macrocephaly, a small amount of anterior parenchyma, a compressed brainstem and posterior fossa, and an abnormal midface. Axial T2 MRI (B) demonstrates fusion of the small volume of brain parenchyma, and the large dorsal cyst. Axial T2 MRI (C) highlights fusion of the deep gray nuclear structures and mesencephalon. Axial T2 MRI (D)at the level of the right orbit shows a dysmorphic orbit with a cephalocele (arrow) but no identifiable globe.

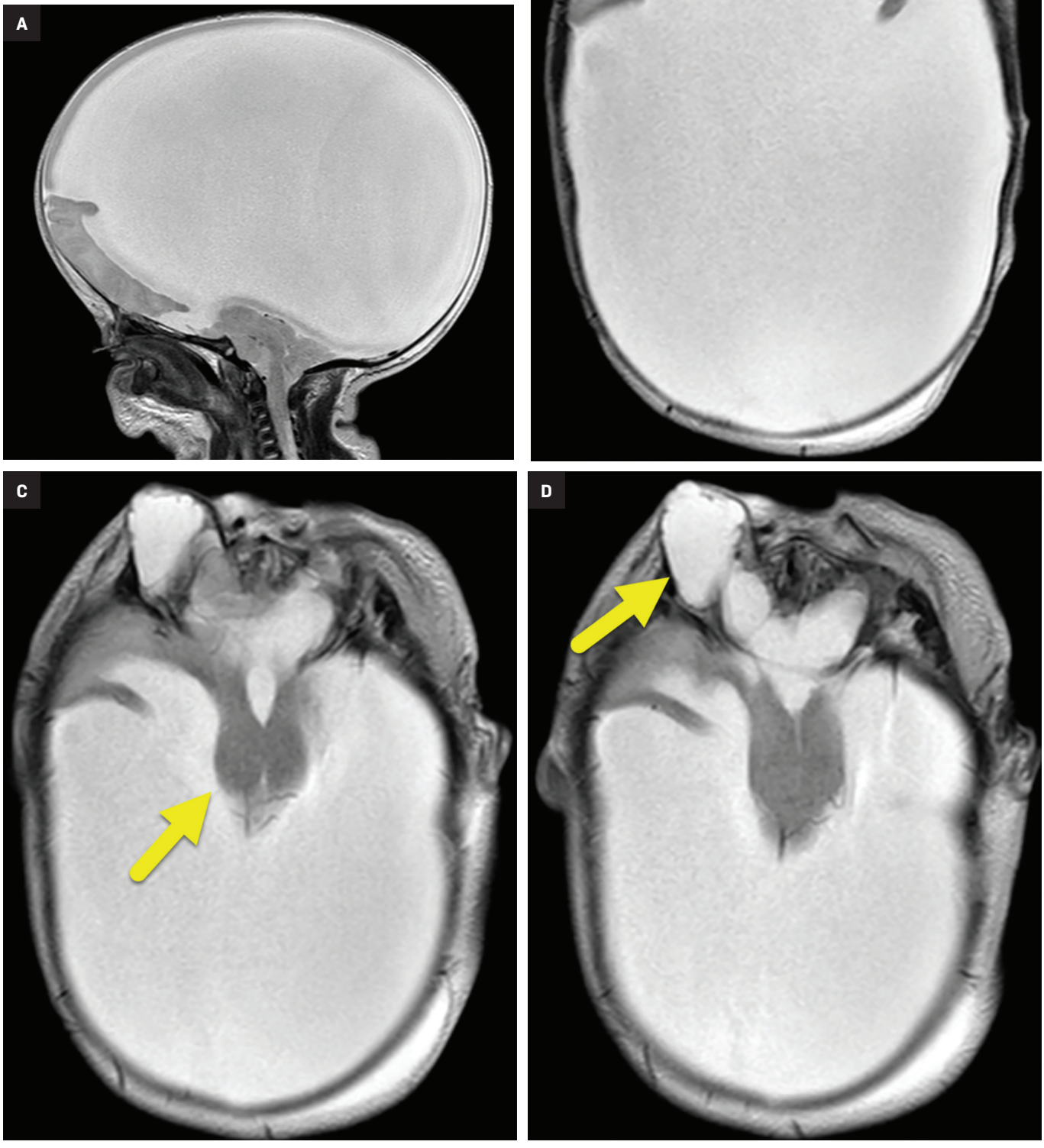

impaired body temperature regulation, and impaired thirst.[8] These patients may develop life-threatening endocrinopathies. Central diabetes insipidus is the most common endocrinopathy in the setting of hypothalamic fusion and absent or dysfunctional hypothalamic-pituitary axis.[10] Patients should also be evaluated for anterior pituitary hormone deficiencies such as hypothyroidism, hypoadrenocorticism, and growth hormone deficiency and given hormone replacement therapy as indicated.[10] Prognosis of alobar HPE is very poor, with one study finding that one-half of patients die before 5 months, and 20–30% survive for at least 1 year.[9]

Conclusion

Alobar HPE is the most severe subtype of forebrain malformation. Characteristic brain MRI findings include fusion of cerebral hemispheres and deep gray nuclei in the rostral aspect of the skull, with a single midline ventricle that communicates with a dorsal cyst. Survival beyond infancy is poor, owing to the presence of severe neurologic impairment, seizures, craniofacial abnormalities, and multiple endocrinopathies.

References

1) Hahn JS, Barnes PD. Neuroimaging advances in holoprosencephaly: Refining the spectrum of the midline malformation. *Am J Med Genet C Semin Med Genet*. 2010;154C(1):120-132. Doi:10.1002/ajmg.c.30238

2) Dubourg C, Bendavid C, Pasquier L, Henry C, Odent S, David V. Holoprosencephaly. *Orphanet J Rare Dis*. 2007; 2:8. Doi:10.1186/1750-1172-2-8

3) Leoncini E, Baranello G, Orioli IM, et al. Frequency of holoprosencephaly in the International Clearinghouse Birth Defects Surveillance Systems: searching for population variations. *Birth Defects Res A Clin Mol Teratol*. 2008;82(8):585-591. Doi:10.1002/bdra.20479

4) Hahn JS, Plawner LL. Evaluation and management of children with holoprosencephaly. *Pediatr Neurol*. 2004;31(2):79-88. Doi: 10.1016/j.pediatrneurol.2004.03.006

5) Tekendo-Ngongang C, Muenke M, Kruszka P. Holoprosencephaly Overview. In: Adam MP, Ardinger HH, Pagon RA, et al., eds. *GeneReviews®*. Seattle (WA): University of Washington, Seattle; December 27, 2000

6) Raam MS, Solomon BD, Muenke M. Holoprosencephaly: a guide to diagnosis and clinical management. *Indian Pediatr*. 2011;48(6):457-466. Doi:10.1007/s13312-011-0078-x

7) Wong AM, Bilaniuk LT, Ng KK, Chang YL, Chao AS, Wai YY. Lobar holoprosencephaly: prenatal MR diagnosis with postnatal MR correlation. *Prenat Diagn*. 2005;25(4):296-299. Doi:10.1002/pd.1108

8) Levey EB, Stashinko E, Clegg NJ, Delgado MR. Management of children with holoprosencephaly. *Am J Med Genet C Semin Med Genet*. 2010;154C(1):183-190. Doi:10.1002/ajmg.c.30254

9) Barr, M., Jr. and Cohen, M.M., Jr. (1999), Holoprosencephaly survival and performance. *Am. J. Med. Genet.*1999; 89: 116-120. Doi:10.1002/(SICI)1096-8628(19990625)89:2<116:AID-AJMG10>3.0.CO;2-4

10) Hahn JS, Hahn SM, Kammann H, et al. Endocrine disorders associated with holoprosencephaly. *J Pediatr Endocrinol Metab*. 2005;18(10):935-941. Doi:10.1515/jpem.2005.18.10.935

Ewing Sarcoma

Pream Kadevari; Richard B. Towbin; MD, Carrie M. Schaefer, MD; Alexander J. Towbin, MD

Case Summary

A teenager presented with a three-week history of right-sided headaches, double vision, intermittent somnolence, and left lower extremity stinging pain and weakness. Additionally, there was left lower extremity weakness on physical examination. The initial imaging included MRI of the brain and spine. A percutaneous biopsy of the posterior right parietal superficial mass was performed, with a pathologic diagnosis of Ewing Sarcoma (EWS). The primary lesion was later confirmed to arise from the left fibula (not shown) on radiographs, PET/CT and MRI where the soft tissue component was best seen.

Imaging Findings

Brain MRI (Figure 1) demonstrated diffuse calvarial signal abnormality and multiple bilateral epidural and scalp masses, the largest overlying the posterior right parietal bone.

Affiliations: Lincoln Memorial University, DeBusk College of Osteopathic Medicine (Mr Kadevari); Department of Radiology, Phoenix Children's Hospital (Drs Schaefer, R. Towbin); Cincinnati Children's Hospital and University of Cincinnati College of Medicine (Dr A. Towbin)

Spine MRI (Figure 2) demonstrated multiple abnormally contrast-enhancing vertebral bodies and mild loss of height at T9 and T11.

Whole body FDG-PET and axial PET/CT through the thorax performed one year after diagnosis demonstrated multifocal FDG uptake in metastatic pleural-based masses, multiple vertebrae, and bilateral extremities.

Diagnosis

Metastatic Ewing sarcoma.

The differential diagnoses for EWS include osteomyelitis and osteosarcoma, both of which can have similar clinical presentations and appear similarly on imaging. Noteworthy imaging features of EWS may help distinguish EWS from these other common bone lesions. When comparing EWS to osteosarcoma, on radiography osteosarcoma typically has mixed lytic and sclerotic destructive bone changes with a periosteal reaction generally perpendicular to the diaphyseal cortex. In contrast, EWS is significantly more likely to show metadiaphyseal involvement.[1,2] Other noteworthy but not pathognomonic characteristics of EWS on radiography include an "onion-skinning" periosteal bone pattern, "hair on end" appearance, and cortical saucerization.[1,2]

Osteomyelitis may be best differentiated from EWS on MRI. EWS is significantly more likely to show heterogeneous cystic and necrotic areas with a contrast-enhancing soft tissue mass, a wide transition zone, and permeative cortical involvement.[1,2] EWS will not show the serpiginous tracks that may be appreciated in osteomyelitis.[2] When comparing the low signal intensity of altered bone on T1 to the hyperintense signal of normal marrow on STIR images, the margins between normal bone and affected regions tend to be more sharply defined in EWS when compared to osteomyelitis.[3]

Discussion

Ewing sarcoma is a malignant tumor of childhood that is described by a t(11;22)(q24;q12) translocation and "small round blue cells" on histology.[6] Ewing sarcoma has an annual incidence of one case per million in the United states with peak morbidity occurring between 15-18 years of age.[7] While similar in histological appearance, EWS is distinct from primitive neuroectodermal tumors, since these tumors lack the *MIC2* gene and do not

Figure 1. (A) Brain MRI axial T2 demonstrating diffuse osseous signal heterogeneity and multiple bilateral epidural and scalp masses, the largest overlying the posterior right parietal bone (arrow). The epidural component partially compressed the posterior aspect of the superior sagittal sinus. (B) Brain MRI axial T1 postcontrast with fat suppression demonstrating heterogeneously enhancing diffuse osseous lesions with epidural (*) and scalp extension (arrows). Areas without enhancement (blue star) reflect necrosis.

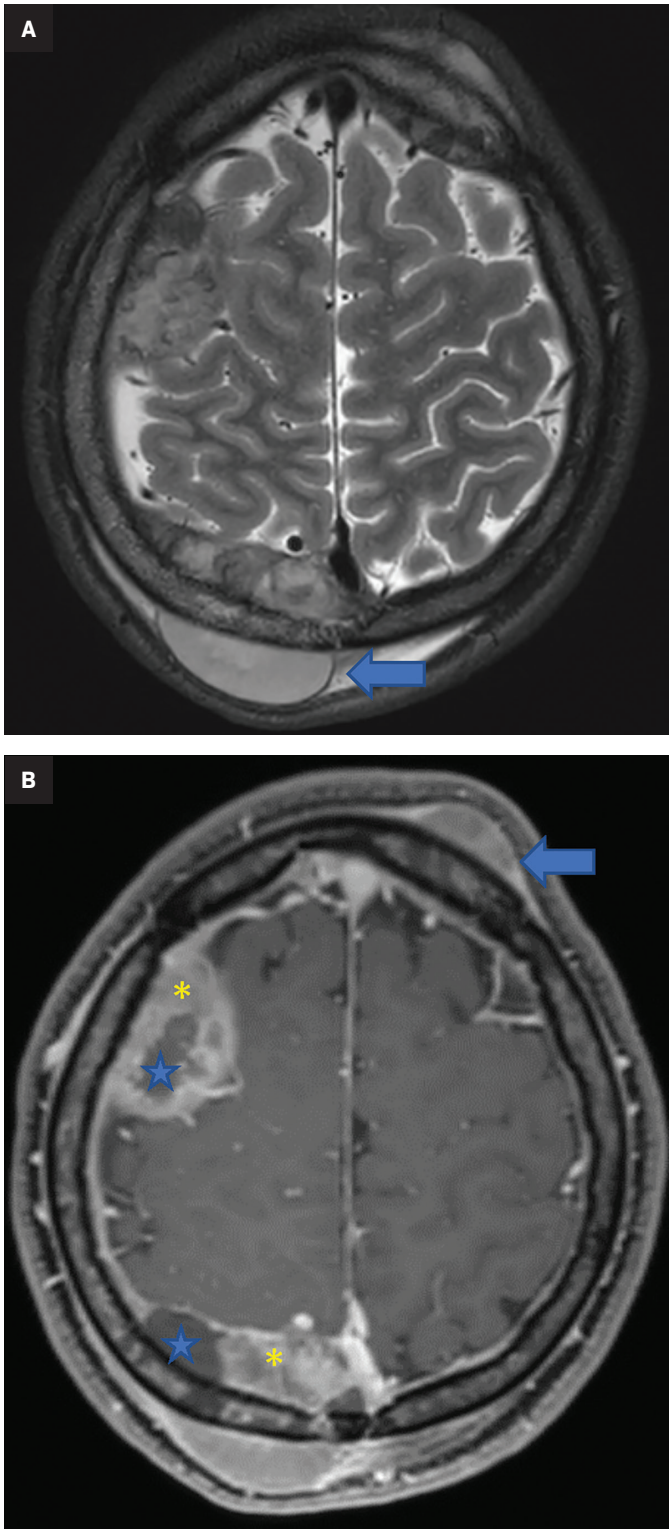

Figure 2. Spine MRI T1 postcontrast with fat suppression demonstrating multiple enhancing vertebral bodies with loss of height at the T9 and T11 levels (*).

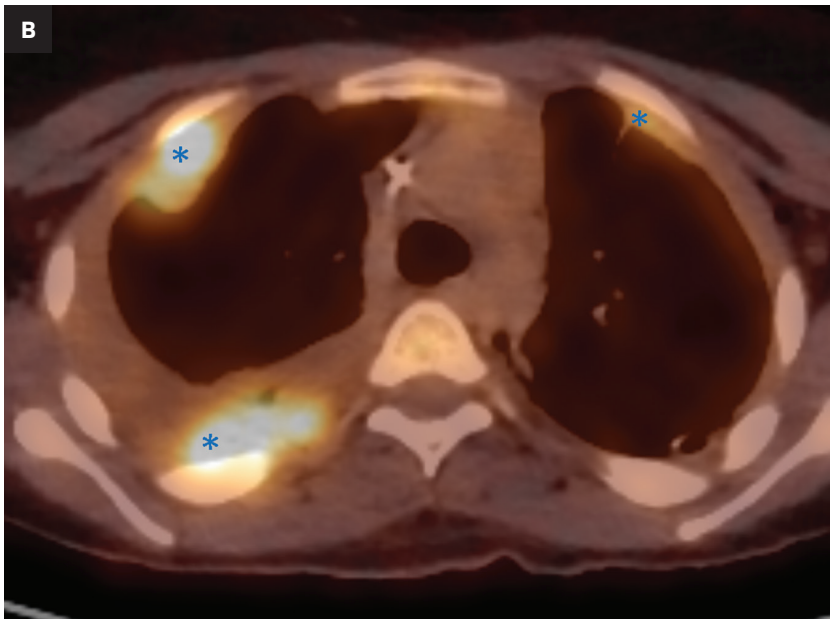

Figure 3. (A) Whole body FDG-PET and (B) axial PET/CT through thorax one year after diagnosis demonstrate multifocal FDG uptake in metastatic pleural-based masses (asterisks), multiple vertebrae, and bilateral extremities (arrows). Note the recurrent large soft tissue mass in the right lateral calf region.

express CD99.[4] Primary EWS most commonly arises in the diaphysis of long bones but may also present in the ribs, flat bones of the pelvis, and spinal column.[6] Distant metastasis most commonly occurs in the lungs (38%), spine (31%), and bone marrow (11%), with skull metastasis being the rarest presentation, occurring in only 2-9% of cases.[8,9]

Definitive diagnosis of EWS can be made with cytogenetic testing for the *EWSR1* gene, which acts as a transcription factor created by fusion of the *EWS* gene located on 22q12 and friend of leukemia virus integration 1 (*FLI1*) gene, located on 11q24, forming a t(11;22)(q24;q12) *EWS-FLI1* translocation.[4] Cell surface protein CD99, though highly sensitive for EWS, is a non-specific marker also seen in lymphoblastic lymphoma, rhabdomyosarcoma, and ependymoma.[4] The presence of other reported markers in combination with CD99, such as NKX2-2, a downstream target of *EWS-FLI1*, is highly specific for EWS.[5] These markers can aid in the differentiation of EWS from other closely related head and neck malignancies such as adamantinoma-like Ewing sarcoma that cannot be differentiated on imaging.[5]

Clinical features include non-specific constitutional signs and symptoms such as fever, anemia, fatigue, nausea, and vomiting.[6,8,9] In the case of calvarial involvement, local symptoms include headache and papilledema due to high intracranial pressures, ear drainage, facial muscle weakness and paralysis. An enlarging, often immobile, non-tender mass may be present on examination.[6,8,9] Lab values may reveal neutrophilia and leukocytosis.[6]

Radiographic features of EWS show bone destruction with an associated large soft tissue mass. The associated bone destruction has a multilayered "onion-skin" like pattern of new periosteal bone formation.[6] However, this finding is not usually appreciated on skull lesions and has otherwise been reported as a lytic mass with mottled bone destruction.[8] MRI findings of primary cranial EWS appear as hypointense on T1, and hypo- to hyperintense on T2.[9] Affected bone margins have very low signal intensity on T1 images, while normal bone has a high signal intensity on T2 or STIR images, which creates a sharply defined margin helping to distinguish EWS from other primary malignant bone tumors.[3]

For evaluation of the primary lesion and osseous metastasis, the

Children's Oncology Group recommends obtaining imaging studies both at time of presentation, at baseline once local control has been achieved, surveillance while on chemotherapy, and upon completion of the treatment regimen. Anterior-posterior and lateral radiographs as well as contrast-enhanced MRI or CT are often the initial imaging studies. Technetium-99m-methylene-diphosphonate bone scintigraphy or Fluorodeoxyglucose PET is the modality of choice for whole body evaluation.

Treatment for EWS involves chemotherapy in combination with radiotherapy. The standard chemotherapeutic protocol typically includes vincristine, doxorubicin, cyclophosphamide, ifosfamide and etoposide.[9] Radiotherapy may be used in combination with surgery, as warranted.[6]

Conclusions

Ewing sarcoma with skull metastasis is a rare occurrence. The aggressive nature of this tumor and poor prognosis in the case of skull metastasis makes early detection and treatment paramount.

Characteristic findings of EWS on plain radiograph can help in differentiating EWS from osteosarcoma, while MRI can aid in distinguishing EWS from osteomyelitis. Imaging is essential for locating the lesion(s), establishing a baseline, and monitoring for recurrence throughout and following the course of treatment. Definitive diagnosis of EWS can be made with cytogenetic testing.

References

1) Heare T, Hensley MA, Dell'Orfano S. Bone tumors: osteosarcoma and Ewing's sarcoma. *Curr Opin Pediatr*. 2009;21(3):365-372. doi:10.1097/MOP.0b013e32832b1111

2) McCarville MB, Chen JY, Coleman JL, et al. Distinguishing Osteomyelitis from Ewing sarcoma on radiography and MRI. *AJR Am J Roentgenol*. 2015;205(3):640-651. doi:10.2214/AJR.15.14341

3) Henninger B, Glodny B, Rudisch A, et al. Ewing sarcoma versus osteomyelitis: differential diagnosis with magnetic resonance imaging. *Skeletal Radiol.* 2013;42(8):1097-104. doi: https://doi.org/10.1007/s00256-013-1632-5

4) Yang MJ, Whelan R, Madden J, et al. Intracranial Ewing sarcoma: four pediatric examples. *Childs Nerv Syst*. 2018;34(3):441-448. doi:10.1007/s00381-017-3684-7

5) de Alva E, Marcilla D, Biscuola M. *Practical Soft Tissue Pathology: A Diagnostic Approach* (Second Edition). Elsevier, 2019. https://doi.org/10.1016/B978-0-323-49714-5.00008-9.

6) Ye C, Wei W, Tang X, et al. Sacral Ewing sarcoma with rib, lung, and multifocal skull metastases: A rare case report and review of treatments. *Front Oncol.* 2022;12:933579. Published 2022 Sep 8. doi:10.3389/fonc.2022.933579

7) Khan S, Abid Z, Haider G, et al. Incidence of Ewing's sarcoma in different age groups, Their associated features, and its correlation with primary care interval. *Cureus.* 2021;13(3): e13986. doi:10.7759/cureus.13986

8) Rana K, Wadhwa V, Bhargava EK, Batra V, Mandal S. Ewing's sarcoma multifocal metastases to temporal and occipital bone: A rare presentation. *J Clin Diagn Res.* 2015;9(6):MD04-MD5. doi:10.7860/JCDR/2015/13254.6071

9) Moschovi M, Alexiou GA, Tourkantoni N, et al. Cranial Ewing's sarcoma in children. *Neurol Sci*. 2011;32(4):691-694. doi:10.1007/s10072-011-0509-4

Acute Wallerian Degeneration

Aaron C. Llanes; Richard B. Towbin, MD; Carrie M. Schaefer, MD; Alexander J. Towbin, MD

Case Summary

A term infant was born via emergency cesarean for fetal bradycardia. The neonate had Apgar scores of 0, 3, and 3 at 1, 5, and 10 minutes of age, respectively. Arterial umbilical cord gas showed a markedly low pH (6.510) and metabolic acidosis (base deficit 30.7) and the child was resuscitated. Physical examination revealed extreme hypotonia. The child was placed on a total body cooling protocol.

Imaging Findings

Brain MRI on day of life 19 demonstrated moderate lateral and third ventricular enlargement, diffuse bilateral periventricular white matter injury, and cortical and deep gray matter injury. In addition, restricted diffusion involved the entirety of the corticospinal tracts (CSTs), from the perirolandic cortices through the upper cervical spinal cord (Figure 1).

Affiliations: University of Arizona College of Medicine-Phoenix Campus (Mr Llanes); Department of Radiology, Phoenix Children's Hospital (Drs Schaefer, R. Towbin); Children's Hospital Medical Center, Cincinnati, University of Cincinnati College of Medicine (Dr A. Towbin).

Diagnosis

Acute Wallerian degeneration.

Differential diagnosis includes traumatic injury, neurodegenerative disease, hemorrhage, cerebral infarction.

Discussion

Wallerian degeneration (WD) refers to the phenomenon of secondary degeneration of the associated axons and myelin sheaths in response to neuronal injury. The condition occurs in both the central and peripheral nervous systems as a reaction to axonal injury resulting from pathology, trauma, or neurodegeneration.[1,2] However, neonatal brain injury is a common cause of WD and most often results from a profound hypoxic-ischemic injury, although neonatal arterial infarction, infection, and inflammation can also be causative. Regardless of etiology, the reaction proceeds through four distinct stages (Table 1).[4]

It has long been known that Schwann cells in the peripheral nervous system (PNS) and oligodendrocytes in the central nervous system (CNS) recruit macrophages and microglia, respectively, to clear microscopic debris resulting from axonal injury.[6] Particularly in CNS-WD, recruitment of oligodendrocytes and microglia is also necessary for the formation of a glial scar, also known as gliosis.[7] The clearance of molecular debris through phagocytosis is mediated by the interactions of complement receptor-3 (CR3) and scavenger receptor-AI/II (SRA) with complement-opsonized myelin.[4]

Additionally, interactions between CD47 on oligodendrocytes and signal-regulatory-protein-α (SIRPα) on healthy myelin are crucial for the inhibition of phagocytosis.[4] Other discoveries have highlighted the role of modifier genes such as nicotinamide mononucleotide adenylyltransferase1 (*NMNAT1*) and sterile alpha and TIR motif containing 1 (*SARM1*) on WD initiation and the speed of the process.[3] These genes hold potential as targets for further exploration of neurologic pathology, as well as candidates for therapy within translational research to promote axonal regeneration in CNS injury.

MRI has contributed to a better understanding of WD.[8] Early studies of WD visualization demonstrated changes in signal intensities on diffusion-weighted MRI over weeks and months in patients who suffered cerebrovascular accidents to assess suspected WD.[9] Additionally, studies have explored the potential of

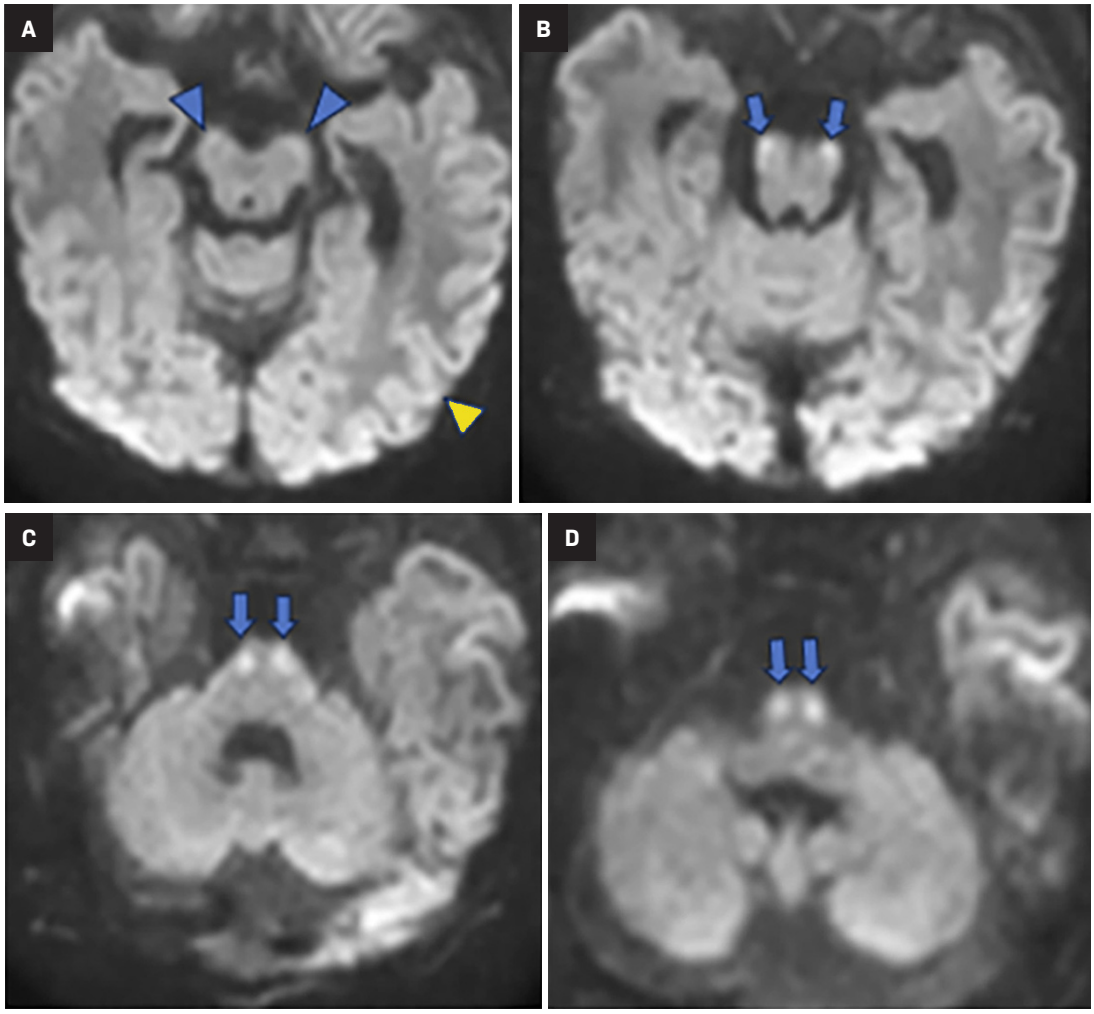

Figure 1. Acute Wallerian degeneration following severe brain injury. Axial B1000 images demonstrate abnormally hyperintense signal in the descending corticospinal tracts in the: (A) anterior aspect of the cerebral peduncles (blue arrowheads). Note the cortical injury (yellow arrowhead); (B) inferior midbrain just above pontine junction (arrows); (C) pons (arrows); and (D) medulla (arrows).

Table 1: Stages of WD Involving the Descending Corticospinal Tract.

STAGE	DESCRIPTION	T1 MRI	T2 MRI	TIME
1	Axonal and myelin sheath degeneration (Acute)	No changes	No changes	0-4 weeks
2	Rapid protein destruction	Hyperintense	Hypointense	4-14 weeks
3	Gliosis and lipid destruction	Hypointense	Hyperintense	> 14 weeks
4	Atrophy of the injured white matter tract(s)	Volume loss of tract(s)	Volume loss of tract(s)	Months to Years

diffusion-weighted MRI to depict acute injury to descending CSTs not visible on CT or structural MRI sequences.[10]

These techniques have also proven valuable in prognostication of deficits and outcomes in WD. Although outcome of perinatal WD varies, as a rule, degree of impairment is highly associated with the degree of axonal damage and is also dependent on the regions affected. Groenendaal, *et al*, demonstrated a strong association between MRI-documented, acute Wallerian degeneration in neonates with hypoxic-ischemic injury and motor abnormalities.[5]

Hayakawa and colleagues found[11] that acute WD detected on diffusion weighted imaging occurred in the CSTs and corpus callosum. Diffusion restriction in both areas was more often noted in the second week of life. The clinical outcome was unfavorable in infants with CST involvement.[11] Greater degrees of hyperintense signal on T2 were associated with lower scores of evoked potentials, indicating loss of function.

While the process of WD has not yet been fully elucidated, efforts have been made to further understanding. For instance, a case report by Szymanski, *et al*, suggests that WD can occur before MRI-visible myelination, as they observed in the CSTs of a deceased neonate, challenging

previous assertions that WD requires myelinated axons.[12]

Conclusion

Wallerian degeneration is a physiological response to axonal injury. The process involves the disintegration of the axons connected to the injury by fiber tracts. Acute WD can be identified with diffusion weighted imaging in the first two weeks of life and can be predictive of neurologic outcome.

References

1) Vargas ME, Barres BA. Why is Wallerian degeneration in the CNS so slow? *Annu Rev Neurosci*. 2007;30:153-179. doi:10.1146/annurev.neuro.30.051606.094354

2) Gaudet AD, Popovich PG, Ramer MS. Wallerian degeneration: gaining perspective on inflammatory events after peripheral nerve injury. *J Neuroinflammation*. 2011;8:110. doi:10.1186/1742-2094-8-110

3) Conforti L, Gilley J, Coleman MP. Wallerian degeneration: an emerging axon death pathway linking injury and disease. *Nat Rev Neurosci*. 2014;15(6):394-409. doi:10.1038/nrn3680

4) Rotshenker S. Wallerian degeneration: the innate-immune response to traumatic nerve injury. *J Neuroinflammation*. 2011;8:109. doi:10.1186/1742-2094-8-109

5) Groenendaal F, Benders MJ, de Vries LS. Pre-wallerian degeneration in the neonatal brain following perinatal cerebral hypoxia-ischemia demonstrated with MRI. *Semin Perinatol*. 2006;30(3):146-150. doi:10.1053/j.semperi.2006.04.005

6) Chen P, Piao X, Bonaldo P. Role of macrophages in Wallerian degeneration and axonal regeneration after peripheral nerve injury. *Acta Neuropathol (Berl)*. 2015;130(5):605-618. doi:10.1007/s00401-015-1482-4

7) Boissonnas A, Louboutin F, Laviron M, et al. Imaging resident and recruited macrophage contribution to Wallerian degeneration. *J Exp Med*. 2020;217(11):e20200471. doi:10.1084/jem.20200471

8) Chen YJ, Nabavizadeh SA, Vossough A, Kumar S, Loevner LA, Mohan S. Wallerian degeneration beyond the corticospinal tracts: conventional and advanced MRI findings. *J Neuroimaging Off J Am Soc Neuroimaging*. 2017;27(3):272-280. doi:10.1111/jon.12404

9) noue Y, Matsumura Y, Fukuda T, et al. MR imaging of Wallerian degeneration in the brainstem: temporal relationships. *AJNR Am J Neuroradiol*. 1990;11(5):897-902. Accessed June 12, 2022. https://www.ncbi.nlm.nih.gov/pmc/articles/PMC8334089/

10) Mazumdar A, Mukherjee P, Miller JH, Malde H, McKinstry RC. Diffusion-weighted imaging of acute corticospinal tract injury preceding Wallerian degeneration in the maturing human brain. *AJNR Am J Neuroradiol*. 2003;24(6):1057-1066. Accessed June 11, 2022. https://www.ncbi.nlm.nih.gov/pmc/articles/PMC8149020/

11) Hayakawa k, Tanda K, Nishimura A, Koshino S, Kizaki Z, Ohno K. Diffusion restriction in the corticospinal tract and the corpus callosum of term neonates with hypoxic-ischemic encephaolpathy. *Pediatr Radiol*. 2022; 52:1356-1369. https://doi.org/10.1007/s00247-022-05331-9

12) Szymanski LJ, Hawes D, Gilles F. Corticospinal Wallerian degeneration before myelination: a case report. *Pediatr Dev Pathol Off J Soc Pediatr Pathol Paediatr Pathol Soc*. 2020;23(5):399-403. doi:10.1177/1093526620923452